Case study: A GPR survey on a morainic lake in northern Italy for bathymetry, water volume and sediment characterization

Title: APPGEO1855

Case study: A GPR survey on a morainic lake in northern Italy for bathymetry, water volume and sediment characterization.

Authors:

Luigi Sambuelli, Silvia Bava.

Affiliation:

Politecnico di Torino
Dipartimento di Ingegneria del Territorio, dell'Ambiente e delle Geotecnologie

Address:

C.so Duca degli Abruzzi, 24 - 10129 – Torino – Italy

Reference Author:

Luigi Sambuelli

e-mail: luigi.sambuelli@polito.it

Keywords: GPR; Sediment porosity, Lacustrine

Abstract

We carried out an extensive waterborne GPR survey consisting of 50 profiles with a total length of nearly 37 km on the morainic lake of Candia northerly Turin (Italy). Our aim was to test the capability of GPR to estimate the bathymetry, the water volume and the sediment type. We enhanced and controlled the GPR data processing and interpretation with bathymetry acquired with an acoustic echo sounder and measured conductivity and temperature profile of the water column with a multiparametric probe. We also analysed the diffraction hyperbola that originated within the sediments in order to estimate the velocity and relative permittivity. With the permittivity and dielectric mixing rules, we estimated the porosity of the sediments above the diffracting objects and drew a map of the bottom lake porosity.

1. Introduction

Here we discuss an extensive waterborne GPR survey of a morainic lake in northern Italy that we performed along with an echo-sounder and spotted measurements along the water column with a multiparametric sonde. The survey aimed to evaluate the capability of a non-seismic tool as the GPR to estimate the water volume and the bottom sediment type.

The use of non-seismic methods to investigate sediments beneath shallow freshwater has increased in the last twenty years (Sambuelli and Butler, 2009; Butler, 2009). Monitoring river erosion, lake filling and understanding the connection between surface water and underground water are critical environmental issues. Many publications related to the application of GPR to shallow-water environments can be found in literature. Annan and Davis (1977) and Kovacs (1978) conducted some early applications of GPR in low-conductivity melting water in arctic areas. In such low-conductivity environments a noticeable subbottom penetration in water depths exceeding 25 m can be achieved (Delaney et al., 1992). Bathymetric maps and sediments morphology of ice-covered lakes (Moorman and Michel, 1997; Schwamborn et al., 2002) rivers and reservoirs (Arcone et al., 1992; Best et al., 2005; Hunter et al., 2003) have been reported as well. In temperate areas GPR has been tested for monitoring stream discharge (Haeni et al., 2000; Melcher et al., 2002; Cheng et al., 2004; Costa et al., 2006), studying bottom deposits (Arcone et al., 2006; Buynevich and Fitzgerald, 2003; Fuchs et al., 2004; Shields et al., 2004; Moorman et al., 2001, Sambuelli et al., 2009), mapping bathymetry (Powers et al., 1999) and subbottom strata (Arcone et al., 2010).

GPR could provide complementary information to seismic methods, especially in very shallow water where reverberation can prevent the interpretation of subbottom reflectors or when gas pockets in sediments rich in organic matter block seismic signal penetration (Delaney et al., 1992; Schwamborn et al., 2002; Arcone et al., 2006; Mellet, 1995). Waterborne GPR can be used in many different setups: case histories report the use of antennas directly coupled to water from the surface (Mellet, 1995; Sellmann et al., 1992), noncontact systems such as helicopter mounts (Melcher et al., 2002) or hanging slings (Haeni et al., 2000; Cheng et al., 2004; Costa et al., 2000), and antennas mounted on the bottom of non-metallic boats (Sambuelli et al., 2009; Sellmann et al., 1992, Bradford et al., 2005; Jol and Albrecht, 2004; Porsani et al., 2004; Park et al., 2004). The potential of GPR to allow estimates bottom sediment types has been mentioned by Ulriksen (1982), who suggested that fine sediments can be identified from smooth reflectors, rough surfaces such as moraine can be identified from speckled and weak signals, while boulders may produce hyperbolic diffractions. As a rule of thumb the coarser is the sediment then the higher are the amplitudes of the reflected GPR signals. The same qualitative approach to the analysis of basin-bottom characteristics has been tested positively by other authors (Mellet, 1995, Beres and Haeni, 1991). In particular,

Dudley and Giffen (1999) found optimal agreement between GPR results and direct sampling of sediments. Recently some more quantitative approaches to the discrimination of sediment type using the amplitude of the GPR signal reflected from the water bottom have been proposed (Sambuelli et al., 2009; Lin et al., 2010).

Estimating the bathymetry and discriminating sediment types by analysing the time delay and amplitude of reflections mainly assumes that the water is homogeneous. This assumption is valid in shallow rivers or lakes where there is little or no thermocline and therefore no reflectors before the bottom, but must be questioned for deeper lakes (Bradford et al., 2007).

2. Site description

The lake of Candia (Turin, Italy) is an example of inter-moraine lake belonging to the morainic amphitheatre of Ivrea, northerly the town of Turin (**Figure 1**). The lake (226 m a.s.l.) has a surface of about 1.52 km^2, a perimeter of about 5.5 km and an estimated volume of about 7.2 Mm^3. The amphitheatre was built up by the Balteo Glacier which flowed through the Aosta Valley during the Quaternary period. The Balteo Glacier had an average width of 3 km, a thickness of around 600 m and was spread over 300 km through the Alps. At its maximum expansion it went down to 25 km into the Po plain with a width of about 20 km, reaching today's northern border of the town of Turin. According to recent studies the lake of Candia was left after the recession of the Riss Glaciation (about 150000 years ago). The lake of Candia then settled in a plain that was eroded by the advancing glacier and then refilled to a far lower extent by the glacial deposits of the glacier retreat. According to Gianotti et al. (2008), the Candia lake lies on the Piverone alloformation (Late Pleistocene) above the Serra alloformation (end of the Middle Pleistocene) each one referable to a different glacial episode.

A borehole (Alice Superiore borehole) drilled about 20 km NNW in the same geological environment gave the stratigraphic log reported in **Figure 2**. It is evident the dominance of more or less dense gravels with boulders that may be included in the mud. A palustrine gyttja layer made by peaty brown clay represents the interstadial episode between the two glacial events. Until about 50 years ago, before an eutrophication process took place, it was possible to see the white gravels of the lake bottom and the fresh water columns rising up to the surface of the lake from underwater springs. Today, the silts and the vegetation prevent the view of the lake bottom. The lake has neither affluent nor effluent but a small ditch used sometimes for irrigation; the water recharge is from rains and underwater springs.

3. Methods

3.1 Data acquisition

We acquired the GPR data with a K2 Ids radar and a Subecho-70 monostatic antenna with peak frequency in air at 89 MHz. We placed the antenna at the bottom of a fiber-reinforced plastic boat and the routes of the profiles were planned and tracked with a Garmin GPS60. We acquired 50 GPR profiles for a total length of about 37 km (**Figure 3**) at a sampling frequency of 1.7 GHz, trace length of 600 ns and a traces interval of 4 cm. Neither filters nor gains were used during the acquisition.

We also acquired bathymetry with a 170kHz Airmar DT800 echo sounder. The dominant wavelength in water roughly equalled 1 cm, and our average sampling interval was 1 m. The echo sounder probe was fixed at the side of the boat and approximately aligned with the centre of the GPR antenna. We also used a Hydrolab Datasonde 4 Multi-Parametric Probe (MPP) to measure temperature, T, and conductivity, σ , along the water column at three points on the lake (**Figure 3**).

3.2 Data processing

We needed to estimate the water conductivity to evaluate the GPR signal attenuation and the water permittivity to evaluate the GPR pulse velocity. We also estimated the dominant frequency of the GPR pulse by doing a spectral analysis of windowed reflected pulses from different water depths. The results shown a dominant frequency range from 66 to 80 MHz with a mode around 70 MHz which was the value selected for further calculations. As a solution to Maxwell's equations the amplitude at a distance z and time t of the electric field $E(z, t, \omega)$ associated with a monochromatic plane wave of angular frequency ω is

$$E(z,t,\omega) = E(z_0,t_0,\omega)e^{i(\omega t+kz)}, \quad (1)$$

where $E(z_0,t_0,\omega)$ is the amplitude at reference time and distance t_0 and z_0. The quantity

$$k_w = i\alpha_w + \frac{\omega}{v_w} \quad (2)$$

is the complex wave number (subscript w refers to water) where

$$\alpha_w = \omega\sqrt{\mu_w\mu_0\frac{\varepsilon_w\varepsilon_0}{2}\left(\sqrt{1+\left(\frac{\sigma_w}{\varepsilon_w\varepsilon_0\omega}\right)^2}-1\right)} \quad (3)$$

and

$$v_w = \frac{1}{\sqrt{\mu_w\mu_0\frac{\varepsilon_w\varepsilon_0}{2}\left(\sqrt{1+\left(\frac{\sigma_w}{\varepsilon_w\varepsilon_0\omega}\right)^2}+1\right)}} \quad (4)$$

are respectively, the attenuation factor due to dissipative phenomena and the phase velocity . Given $\mu_0=4\pi\times10^{-7}$ [H/m], $\mu_w=\mu_0$, $\varepsilon_0=(36\pi)^{-1}\times10^{-9}$ [F/m] and $\omega=2\pi\times70\times10^6$ [rad/s], we need ε_w and σ_w to evaluate α_w and v_w.

The MPP gives the T and σ_w so that we calculated the permittivity using the formula given by Nyshadam et al. (1992):

$$\varepsilon_w = 87.74 - 4.0008\times10^{-1}T - 0.09398\times10^{-2}T^2 - 0.00141\times10^{-3}T^3 \pm 0.009 \qquad 5$$

The average salinity of the lake water was about 0.06 ppt (part per thousand) and so the correction to apply to eq. 5 for such values of salinity is negligible. We plotted the T and the σ_w along the water columns according to the MPP data (**Figure 4 a,b**). The small temperature gradient below the first meter was so small and showed such small variations (**Figure 4 c,d,e**) that we rejected the hypothesis of a thermo cline. We then used the following values of velocity and attenuation in the GPR processing: v_w=0.033 [m/ns] and α_w=2.24 [dB/m].

We processed the GPR profiles with the Reflexw® software. We corrected for the direct arrival delay and eliminated the very low frequency trend. We band-pass filtered from 20 to 190 MHz with a Butterworth filter to attenuate both low and high frequency noise and then resampled the traces to obtain a trace interval of 0.2 m. We removed the steady background horizontal continuous signals with a spatial high-pass filter. We applied firstly a divergence compensation, using v_w, to recover the amplitude attenuation due to the geometrical spreading, and then secondly an exponential gain, using α_w, to recover the amplitude decrease due to the dissipation related to the water conductivity. As far as the wavelength is concerned, the dominant wavelength of the GPR signal bottom reflection ranged from about 0.4 m in the more shallow waters to about 0.5 m in the deepest. To enhance the continuity of the reflectors we then applied a horizontal running average over 11 traces that, giving the new spatial sampling interval, roughly corresponds to a low pass filter that attenuates the wavelengths shorter than 2 m. We then picked the first break of the first bottom reflection to estimate the bathymetry of the lake and to calculate the volume of water. Finally we applied a muting above the picked times to cancel out residual noise in water. In the following some processed radragrams will be presented.

To assess the bathymetry given by the GPR we compared the water depths to those obtained with the acoustic sounder. On average the difference between the two bathymetric data was about 0.17 m with a standard deviation of 0.14 m. This discrepancy could be caused by different reflecting boundaries because the acoustic signal should have no penetration whereas the GPR signal is sensitive to subtle near surface layering. This difference could also be enhanced by the

largely different wavelengths so that the leading edges of the pulses could be differently estimated. It could be also due to the fact that the echo sounder sensor was roughly connected to the boat side and we could not account for the exact depth of the sensor below the water surface nor its rolling and pitching with respect to the boat.

To estimate the bottom sediment porosity we used the diffraction events that later than the bottom lake reflection. The diffractions are caused by point-like objects within the sediments. The t and x coordinates of these events obey the following equations

$$t = \frac{2h_1}{v_1 \cos(i)} + \frac{2h_2}{v_2 \cos(r)} \qquad 6$$

and

$$x = h_1 \tan(i) + h_2 \tan(r), \qquad 7$$

where h_1 is the water depth above the vertex of the diffraction pattern, h_2 is the thickness of sediment above the vertex, i is the incident angle, r is the refracted angle and v_1 and v_2 are, respectively, the velocity of GPR wave in water and in sediment (**Figure 5**). The incident and the refracted angles i and r, v_1 and v_2 are related by Snell' s law

$$\frac{\sin(i)}{\sin(r)} = \frac{v_1}{v_2} \qquad 8$$

For each one of the diffraction events within the radargrams we can read n experimental data pairs (t_e, x_e), $2h_1/v_1$ and $2h_2/v_2$. These latter are respectively, the two-way-traveltime (twt) of the reflection from water-sediment interface above the event vertex (i.e., t_1) and the twt relative to the path within the sediments from the above mentioned point to the vertex of the event (i.e., t_2). However, the two equations [6, 7] cannot be solved for a unique solution in the form $t=t(x)$. Therefore we set up a procedure to determine the unknowns h_2 and v_2 which consists of fitting the (t_e, x_e) with (t, x) obtained from equations [6, 7] by spanning all possible incident angles with values of v_2 ranging from the velocity in water to the velocity in air. We then found the sediment velocity v_2 by searching for the minimum of a misfit function between calculated and experimental traveltimes related to each diffraction event. To have a more robust estimate, less sensitive to outliers, the selected function was the mean absolute difference (*mad*) that is:

$$mad = \frac{\sum |t_e - t|}{N} \quad , \qquad 9$$

where t_e are the experimental picked twt in x_e, t are the calculated twt in x_e and N is the number of twt's considered for each diffraction event. A simplified script referring to the routine implemented for the procedure is reported in Appendix A.

We assessed the effectiveness of this procedure by performing a synthetic test with the finite difference modeller contained in the Reflexw® software. We built a model consisting of a point-like scattering target within sediments under a water layer . The synthetic GPR pulse had a dominant frequency of 100 MHz; the scatter source had a diameter D = 0.16 m and the dominant wavelength of the GPR signal was λ=0.32 m. In **Figure 5** a sketch of the geometry implied in equations 6, 7, 8 with the main physical and geometrical parameters used for the synthetic model is shown. In **Figure 6a, b** the model and the synthetic radargram are respectively shown. The fitting procedure results were ε_2=25.06 and h_2=1.72 m, with a relative percent error with respect to the expected values respectively of 0.24% and 1.16%.

We then selected the clearest diffraction events along the profiles and, according to the proposed procedure, estimated the local porosities. In Figures 7 and 8a, 8b an example of the aforementioned procedure is shown. **Figure 7** shows one of the selected diffraction events observed beneath the bottom sediment. **Figure 8a** shows the trend of the misfit function between calculated and observed data. **Figure 8b** shows the fitting between experimental and calculated (*twt, x*) pairs. Over the 51 diffraction events we analysed we had the following statistical figures: mean(min(mad)) = 0.95 ns, st.dev.(min(mad)) = 1.16 ns. We considered these statistical results positively. In fact the sampling interval during acquisition was 0.588 ns so that the mean of the selected *mad*'s (mean(min(mad))) was less than twice the sampling interval of the radar traces.

We then inserted the v_2 values, converted in the dielectric permittivity of sediments ε_s, in a mixing rule that, given the dielectric permittivity of water and solid particles, allowed the local sediment porosity (Sambuelli, 2009) to be estimated. Among the many mixing formulas available we selected the Maxwell (Equation 10) (Maxwell, 1892) and the so called CRIM (Birchak et al., 1974) which are

$$\phi = 3\varepsilon_w \frac{\varepsilon_s - \varepsilon_{ss}}{(\varepsilon + 2\varepsilon_w)(\varepsilon_w - \varepsilon_s)} \quad , \qquad 10$$

and

$$\phi = \frac{\sqrt{\varepsilon_s} - \sqrt{\varepsilon_{ss}}}{\sqrt{\varepsilon_w} - \sqrt{\varepsilon_{ss}}} \qquad 11$$

respectively, where ϕ is the porosity, ε_s the relative permittivity of the sediments calculated from v_2, ε_w=82 (the relative permittivity of the water taken from the MPP data), and ε_{ss}=6 is an average relative permittivity of the solid grains taken from the literature (Reynolds, 1997; Parkhomenko, 1967). We then averaged the porosities.

4. Results and discussion

The GPR survey shows that the bottom of Candia lake consists of two main types of sediment. One is gravel and pebbles, which shows a high reflectivity and therefore is not penetrated by GPR signal. The other is organic-rich silt, with a lower reflectivity, more transparent, and allows the underlying bedding to be detected. In **Figure 9** we show the radargrams recorded along the red lines in Figure 3. From the top to the bottom of the figure the profiles are from East to West. The gravels are clearly visible as is their progressive cover by the silts going westward. The top radargram, in particular, shows the high reflectivity of the gravels underlain by a multiple reflection. On the other hand the transparency of the silt is clearly depicted by the evident reflection of the gravels beneath the silt. The gravels are likely moraine while the silt (younger) is likely later sedimentation always superimposed on the gravels. We confirmed the outcropping of the gravels and pebbles of the moraine by sampling with a Van Veen grab bucket (**Figure 10a**). We actually found respectively organic rich slime (**Figure 10b**) and pebbles (**Figure 10c**) where the radargrams showed weak and strong reflections.

By converting the twt's of the bottom reflections in water depth and using the velocity of the GPR pulse in water obtained with the MPP, we plotted the bathymetry of the lake (**Figure 11**). The water volume we calculated agreed with the value (about 7 Mm^3) referred to in literature (Comino et al., 2005).

In Figure 12 we show a porosity map of the lake bottom (**Figure 12**). We mapped porosity 0.15 up 0.65. The lowest values are compatible with poorly sorted gravel with sand and silt filling the spaces between the largest grains. The highest value are compatible with silt or fine sand rich in organic material. These unusually high porosity values have also been found in the sea bottom (Ullman and Aller, 1982), and in pond (Avnimelech et al., 2001) and lake bottoms (Hartke and Hill, 1974). Even if the sampled points were few and oddly distributed it seems evident that significant areas of the bottom sediments have porosity larger than 0.55. These areas have a great role in the biological and hydro-geochemical processes developing within the lake.

5. Conclusion

Our three main results are: the identification of an area of the lake bottom made by the coarse materials of the moraine, the bathymetry and water volume and the estimated porosity of the bottom sediments.

The waterborne GPR can be effective to estimate bathymetry of shallow freshwater basins, together with the bedding and porosity of the bottom sediments, provided that the water resistivity, using a GPR central frequency ranging from 50 to 100 MHz, is higher than 40 Ωm to reach 3 to 10 m depths. The depth can be even greater if very low conductivity water derives from ice melting. Profiling of the subbottom bedding largely depends on the bottom sediment type. The finer are the bottom sediments the lower is their reflectivity the higher is the probability to image strata beneath the bottom surface. An estimation of the bottom sediment porosity can also be achieved if point-like scattering targets within the sediments are found. Then our diffraction matching procedure allows an estimation of the GPR pulse velocity in the sediment and hence, with suitable mixing rules, a porosity range for the sediment above the scatterers can be derived.

Appendix A

We present a scheme of the script we wrote to implement the procedure for the determination of the velocity of sediments v_2. The knowns quantities are : t_1, v_1, h_1, $t_2(=h_2/2v_2)$, $\{t_e\}$, $\{x_e\}$. In the script: v_w = velocity in water; v_{air}= velocity in air; t_e = experimental times picked on the diffraction hyperbola; x_e = coordinate related to t_e; r = refraction angle; v_2 = velocity in sediments. The line "spline $(t, x) \rightarrow t(x \mid v_2)$" means that a cubic spline is used to interpolate the calculated (t ,x) and calculate the value of t corresponding to each x_e coordinate.

```
for v2 = vw to vair [200 steps]
        calculate h2
        for r = 0° to 75° [25 steps]
                calculate i (Eq.8)
                calculate t (Eq.6)
                calculate x (Eq.7)
        next r
        spline (t, x)→t(x | v2)
        calculate t(xe | v2)            % calculate the t's after spline interpolation
        read (te) at xe                 % read the experimental data
        calculate mad (Eq.9)            % using t(xe | v2) and te
next v2
plot (v2, mad) (Figure 8a)              % plot mad versus velocity
find v*2 = v2(min(mad))                 % find the velocity corresponding to the minimum mad
plot t(x | v*2) and {xe, te}(Figure 8b) % plot the calculated hyperbola and the experimental data
```

Acknowledgments

The Authors would like to thank the “Ente Parco naturale di interesse provinciale del Lago di Candia” for the permission of working on the lake and publishing the results. Thanks are also due to Alessandro Arato, Mariantonia Zappone, Corrado Calzoni, Stefano Stocco and Diego Franco for their help in collecting and processing data. This study has been founded by MIUR GRANT 2007ET8X4C_002: “GeoElectromagnetic Methods for MApping River Sediments (GEMMARS)” within the project “Groundwater control , protection and management. The contribution of innovative geophysical methods”. Finally the Authors wish to thank the reviewers whose suggestions improved the paper.

References

Annan, A. P., Davis, J. L., 1977. Impulse radar applied to ice thickness measurements and freshwater bathymetry: Report of Activities Part B, Geological Survey of Canada.

Arcone, S. A., Chacho, E. F. J., Delaney, A. J., 1992. Short-pulse radar detection of groundwater in the Sagavanirktok River floodplain in early spring. Water Resources Research, 28, 2925–2936.

Arcone, S. A., Finnegan, D., Laatsch, J. E., 2006. Bathymetric and subbottom surveying in shallow and conductive water. Proceedings of the 11th International Conference on Ground Penetrating Radar, on CDROM.

Arcone, S. A., Finnegan, D., Boitnott, G., 2010. GPR characterization of a lacustrine UXO site. Geophysics, 75, WA221-WA239.

Avnimelech, Y., Ritvo, G., Meijer, L. E., Kochba, M., 2001. Water content, organic carbon and dry bulk density in flooded sediments. Aquacultural Engineering, 25, 25-33.

Beres, M., Haeni, F. P., 1991. Application of ground-penetrating-radar methods in hydrogeologic studies. GroundWater, 29, 375–386.

Best, H., McNamara, J. P., Liberty, L., 2005. Association of ice and river channel morphology determined using ground-penetrating radar in the Kuparuk River, Alaska. Arctic, Antarctic, and Alpine Research, 37, 157–162.

Birchak, J. R., Gardner, C. G., Hipp, J. E, Victor, J. M., 1974. High dielectric microwave probes for sensing soil moisture. Proceedings of the IEEE, 62, 93-98.

Bradford, J. H., McNamara, J. P., Bowden, W., Gooseff, M.N., 2005. Measuring thaw depth beneath peat-lined arctic streams using ground-penetrating radar. Hydrological Processes, 19, 2689–2699.

Bradford, J. H., Johnson, C. R., Brosten, T., McNamara, J. P., Gooseff, M. N., 2007. Imaging thermal stratigraphy in freshwater lakes using georadar. Geophysical Research Letters, 34, 1-5.

Butler, K. E., 2009. Trends in waterborne electrical and EM induction methods for high resolution sub-bottom imaging. Near surface Geophysics, 7, 241-246.
Buynevich, I. V., Fitzgerald, D. M., 2003. High-resolution subsurface GPR Imaging and sedimentology of coastal ponds, Maine, U. S. A.: Implications for Holocene back-barrier evolution. Journal of Sedimentary Research, 73, 559–571.
Cheng, R. T., Gardner, J. W., Mason, R. R. Y., Costa, J., Plant, J., Spicer, K. R., Haeni, F. P., Melcher N. B., Keller, W. C., Hayes, K., 2004. Evaluating a radar-based, non contact streamflow measurement system in the San Joaquin River at Vernalis, California. U. S. Geological Survey.
Comino, E., Quaglino, A., Cerrato, D., 2005. La fitodepurazione come tecnologia per la riduzione del carico eutrofico. Progetto e realizzazione di un impianto, 15th Meeting of the Italian Society of Ecology, Torino, 6 pp.
Costa, J. E., Spicer, K.R., Cheng, R. T., Haeni, F. P., Melcher, N. B., Thurman, E. M., Plant, W. J., Keller, W. C., 2000. Measuring stream discharge by non-contact methods: A proof-of-concept experiment. Geophysical Research Letters, 27, 553–556.
Costa, J. E., Cheng, R. T., Haeni, F. P., Melcher, N. B., Spicer, K. R., Hayes, E., Hayes, K., Plant, W. J., Teague, C., Barrick, D., 2006. Use of radars to monitor stream discharge by noncontact methods. Water Resources Research, 42, W07422, 14pp.
Delaney, A. J., Sellmann, P.V., Arcone, S. A., 1992. Sub-bottom profiling: a comparison of short-pulse radar and acoustic data. Proceedings of the 4th International Conference on Ground Penetrating Radar, 149–157.
Dudley, R.W., Giffen, S. E., 1999. Composition and distribution of streambed sediments in the Penobscot River,Maine. U. S. Geological Survey Water-Resources Investigations Report 01-4223.
Gianotti, F., Forno, M. G., Ivy-Ochs, S., Kubik, P. W., 2008. New chronological and stratigraphical data on the Ivrea amphiteatre (Piedmont, NW Italy). Quaternary International, 190, 123-135.
Fuchs, M., Beres, M. J., Anselmetti, F. S., 2004. Sedimentological studies of western Swiss lakes with high-resolution reflection seismic and amphibious GPR profiling. Proceedings of the 10th International Conference on Ground Penetrating Radar, on CDROM.
Haeni, F. P., Buursink, M. L., Costa, J. E., Melcher, N. B., Cheng, R. T., Plant, W. J., 2000. Ground-penetrating RADAR methods used in surface-water discharge measurements. Proceedings of the 8th International Conference on Ground Penetrating Radar.
Hartke, E. J., Hill, J. R., 1974. Sedimentation in Lake Lemon Monroe County, Indiana. Environmetal study 3, Department of Natural Resource Geological Survey Occasional paper 9, Authority of the state of Indiana, Bloomington, 1-23.

Hunter, L. E., Ferrick, M. G., Collins, C. M., 2003. Monitoring sediment infilling at the Ship Creek Reservoir, Fort Richardson, Alaska, using GPR, in: Bristow, C. S., Jol, H. M., (Eds.), Ground penetrating radar in sediments: Geological Society of London Special Publication 211, 199–206.
Jol, H. M., Albrecht, A., 2004. Searching for submerged lumber with ground penetrating radar: Rib Lake. Proceedings of the 10th International Conference on Ground Penetrating Radar, on CDROM.
Kovacs, A., 1978. Remote detection of water under ice-covered lakes on the North Slope of Alaska. Arctic, 31, 448–458.
Lin, Y. T., Wu, C. H., Fratta, D., Kung, K. J. S., 2010. An integrated acoustic and electromagnetic wave-based technique to estimate subbottom sediments properties in a freshwater environment. Near surface geophysics, 8, 213-221.
Maxwell, J.C., 1892. A treatise on electricity and magnetism, Clarendon Press, Oxford, vol.1.
Melcher, N. B., Costa, J. E., Haeni, F. P., Cheng, R. T., Thurman, E. M., Buursink, M. K., Spicer, R., Hayes, E., Plant, W. J., Keller, W. C., Hayes, K., 2002. River discharge measurements by using helicopter-mounted radar. Geophysical Research Letters, 29, 41-1–41-4.
Mellett, J. S., 1995. Profiling of ponds and bogs using ground-penetrating radar. Journal of Paleolimnology, 14, 233–240.
Moorman,B. J., Michel, F. A., 1997. Bathymetric mapping and sub-bottom profiling through lake ice with ground-penetrating radar. Journal of Paleolimnology, 18, 61–73.
Moorman, B. J., Last, W. M., Smol, J. P., 2001. Ground-penetrating radar applications in paleolimnology, in: Last, W. M., Smol, J. P. (Eds.), Tracking environmental change using lake sediments: Physical and chemical techniques, Kluwer Academic Publishers, Boston, 23–47.
Nyshadham A., Sibbald, C. L., Stuchly, S. S., 1992. Permittivity measurements using Open Ended sensors and reference liquid calibration – an uncertainty analysis. IEEE transaction on microwave theory and techniques, 40, 305-314.
Park, I., Lee, J., Cho, W., 2004. Assessment of bridge scour and riverbed variation by a ground penetrating radar. Proceedings of the 10th International Conference on Ground Penetrating Radar, on CDROM.
Parkhomenko, E. I., 1967. Electrical Properties of Rocks, Plenum, NewYork, pp.314.
Porsani, J. L., Moutinho, L., Assine, M. L., 2004. GPR survey in the Taquari River, Pantanal wetland, west-central Brazil. Proceedings of the 10th International Conference on Ground Penetrating Radar, on CDROM.
Powers, C. J., Haeni, F. P., Spence, S., 1999. Integrated use of continuous seismic-reflection profiling and ground-penetrating radar methods at John's Pond, Cape Cod, Massachusetts.

Proceedings of the Symposium on the Application of Geophysics to Engineering and Environmental Problems SAGEEP.
Reynolds, J., 1997. An Introduction to Applied and Environmental Geophysics, New York, Wiley, pp.796
Sambuelli, L., Butler, K.E., 2009. Foreword, in: Sambuelli, L., Butler, K. E., (Eds), High Resolution Geophysics for Shallow Water, Near surface Geophysics, 7, 3-4. (Special Issue).
Sambuelli L., 2009. Uncertainty propagation using some common mixing rules for the modelling and interpretation of electromagnetic data. Near surface geophysics, 7, 285-296
Sambuelli, L., Calzoni, C., Pesenti, M., 2009. Waterborne gpr survey for estimating bottom-sediment variability: a survey on the Po river, Turin, Italy. Geophysics, 74, B95-B102.
Schwamborn, G. J., Dix, J. K., Bull, J. M., Rachold, V., 2002. High-resolution seismic and ground penetrating radar-geophysical profiling of a thermokarst lake in the western Lena delta, northern Siberia. Permafrost and Periglacial Processes, 13, 259–269.
Sellmann, P. V., Delaney, A. J., Arcone, S. A., 1992. Sub-bottom surveying in lakes with ground penetrating radar. U. S. Army Cold Regions Research and Engineering Laboratory report 92-8.
Shields, G., Grossman, S., Lockheed, M., Humphrey, A., 2004. Waterborne geophysical surveys on shallow river impoundments. Proceedings of the Symposium on the Application of Geophysics to Engineering and Environmental Problems SAGEEP.
Ullman, W. J., Aller, R. C., 1982. Diffusion coefficients in nearshore marine sediments. Limnology and Oceanography, 27, 552-556.
Ulriksen, C. P. F., 1982. Application of impulse radar to civil engineering: Ph.D. dissertation, Lund University of Technology.

Caption of Figures

Figure 1: The location of the Candia Lake in northern Italy.

Figure 2: Stratigraphic log of the Alice Superiore borehole (redrawn from Gianotti et al. [34]).

Figure 3: The violet lines show the GPR profiles. The four yellow lines refer to the profiles (1, 4, 6, 7 from East to West) that are more deeply illustrated in the paper. Yellow pins refer to the locations of the Multi-Parametric Probe measurements.

Figure 4: The vertical profiles of: measured temperatures (a); measured conductivities (b); calculated relative permittivity (c); calculated GPR pulse velocity (d); calculated GPR pulse attenuation (e).

Figure 5: Sketch of the geometrical model used to calculate the GPR pulse velocity in sediments using the diffraction events from objects within the sediments (Equations 6, 7, 8). The electromagnetic and geometrical parameters used in the finite difference synthetic model are also shown.

Figure 6: The synthetic model (a); the synthetic radragram (b).

Figure 7: An experimental diffraction event within the sediments.

Figure 8: Analysis of the event in figure 7. The search for the velocity giving the minimum *mad* (a); the fitting of the calculated (continuous line) and experimental (circles) *twt,x* pairs (b).

Figure 9: The processed radargrams corresponding to the four profiles shown as yellow lines in Figure 3. All the radargrams runs from South to North. On the left (near the South shore) the gravels, and the related multiples, are visible as brighten reflections in all the radargrams. In profiles 6 and 7 the gravels are covered by the silt that fills the great part of the lake bottom.

Figure 10: The direct sampling of the lake bottom. The Van Veen Grab Bucket (a); the silt (b); the pebbles (c).

Figure 11: The bathymetry map of the lake.

Figure 12: The porosity map of the lake sediments. The black crosses refer to the points were we found the analyzed diffraction events within the sediments.

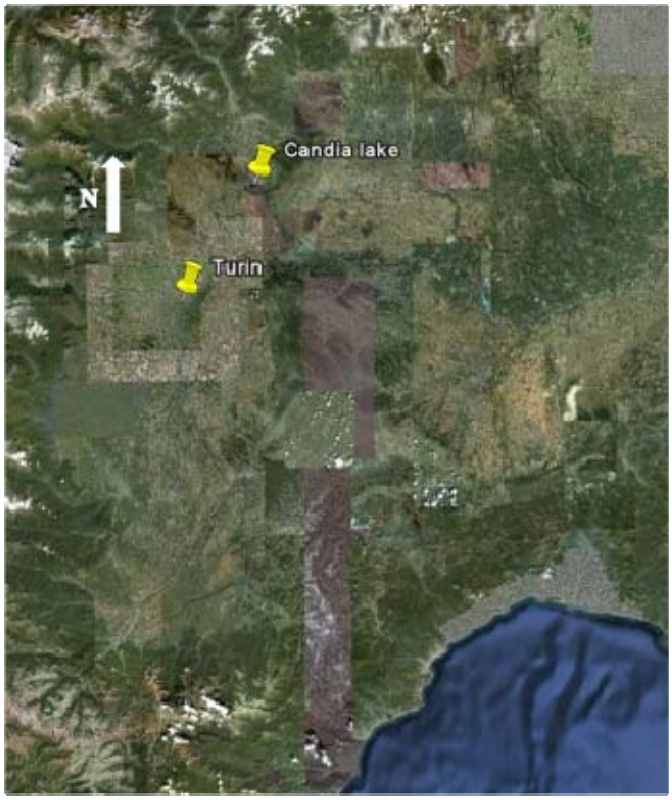

Figure 1

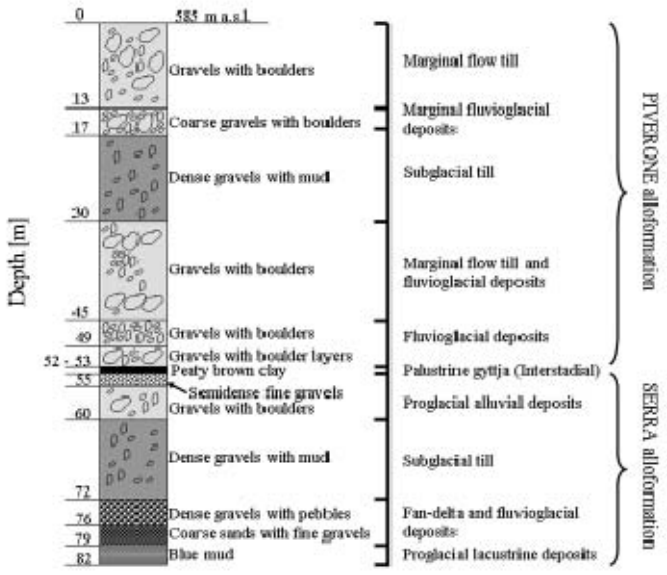

Figure 2

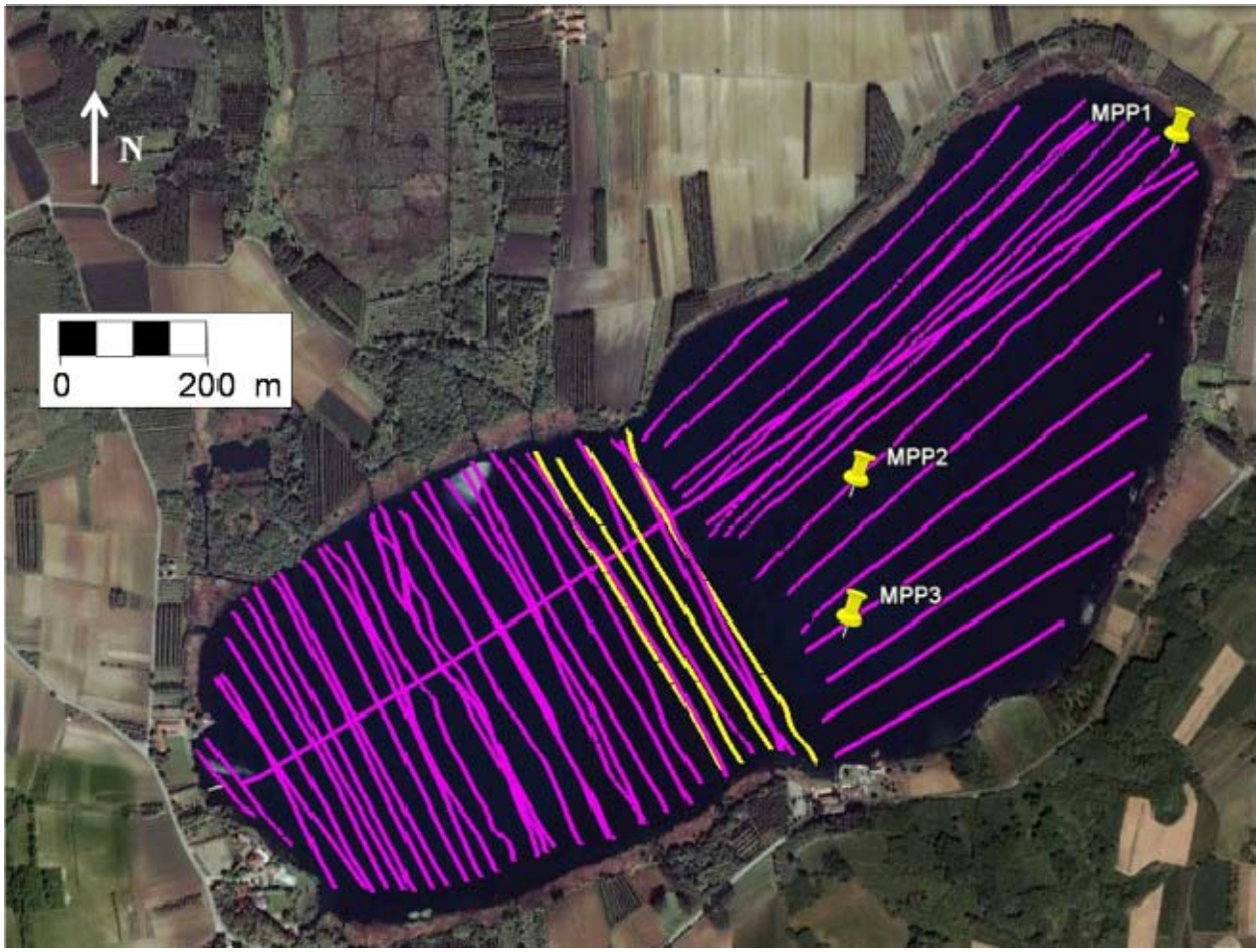

Figure 3

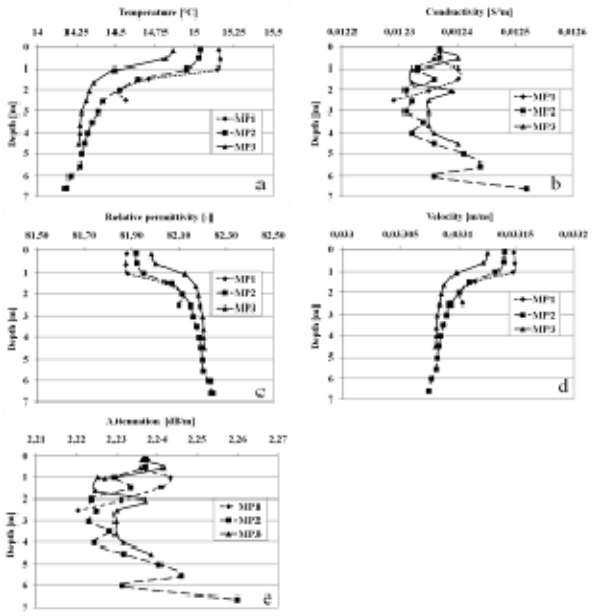

Figure 4

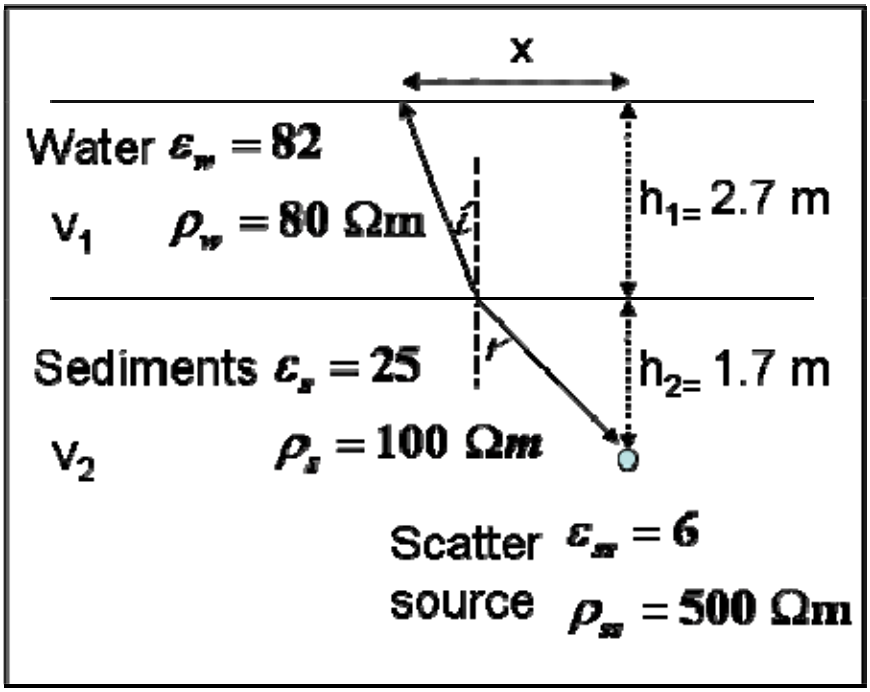

Figure 5

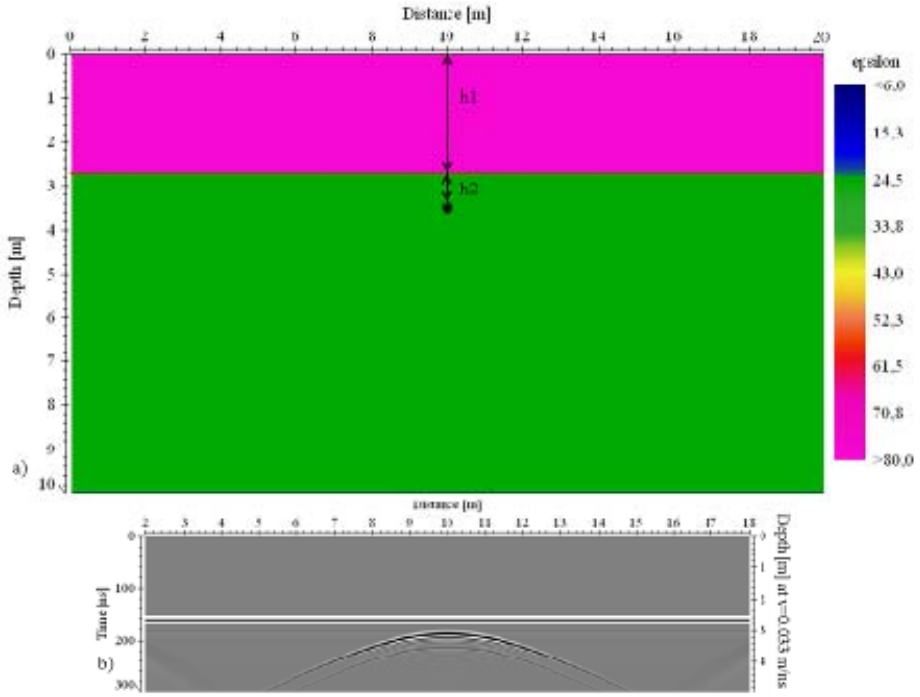

Figure 6

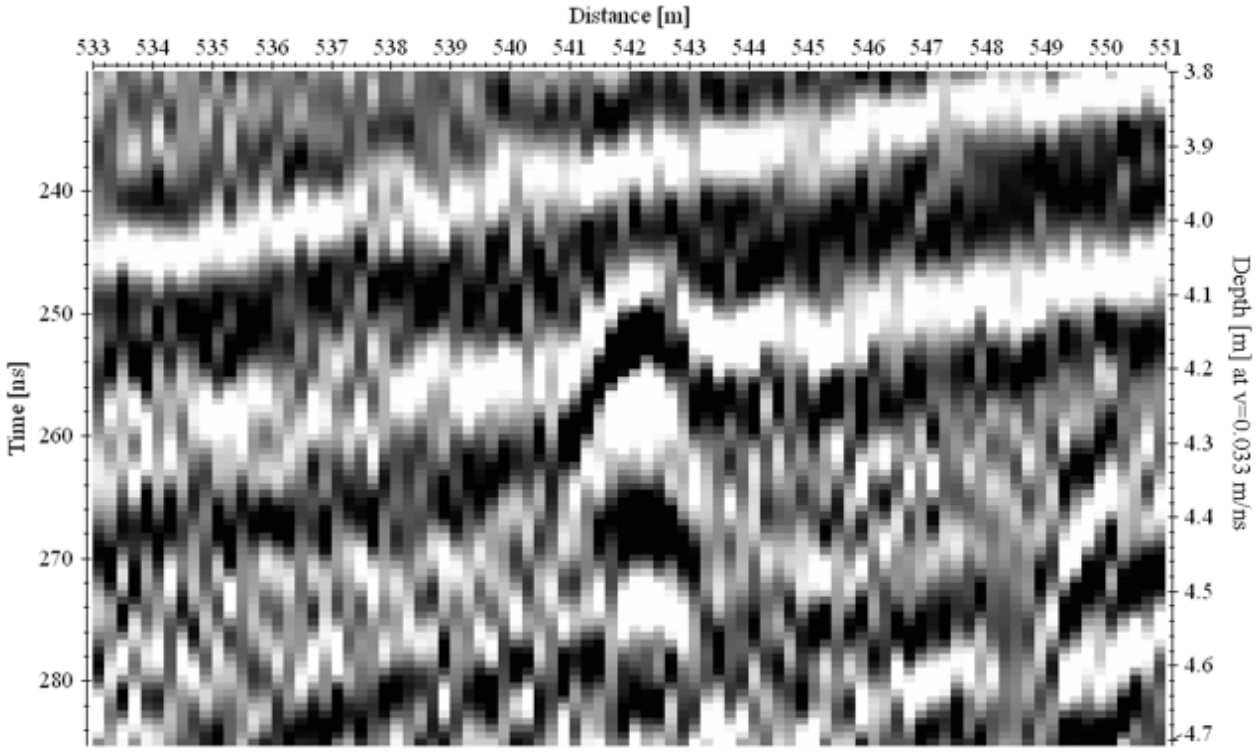

Figure 7

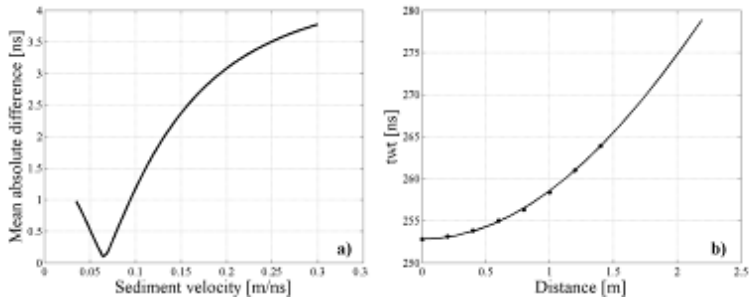

Figure 8

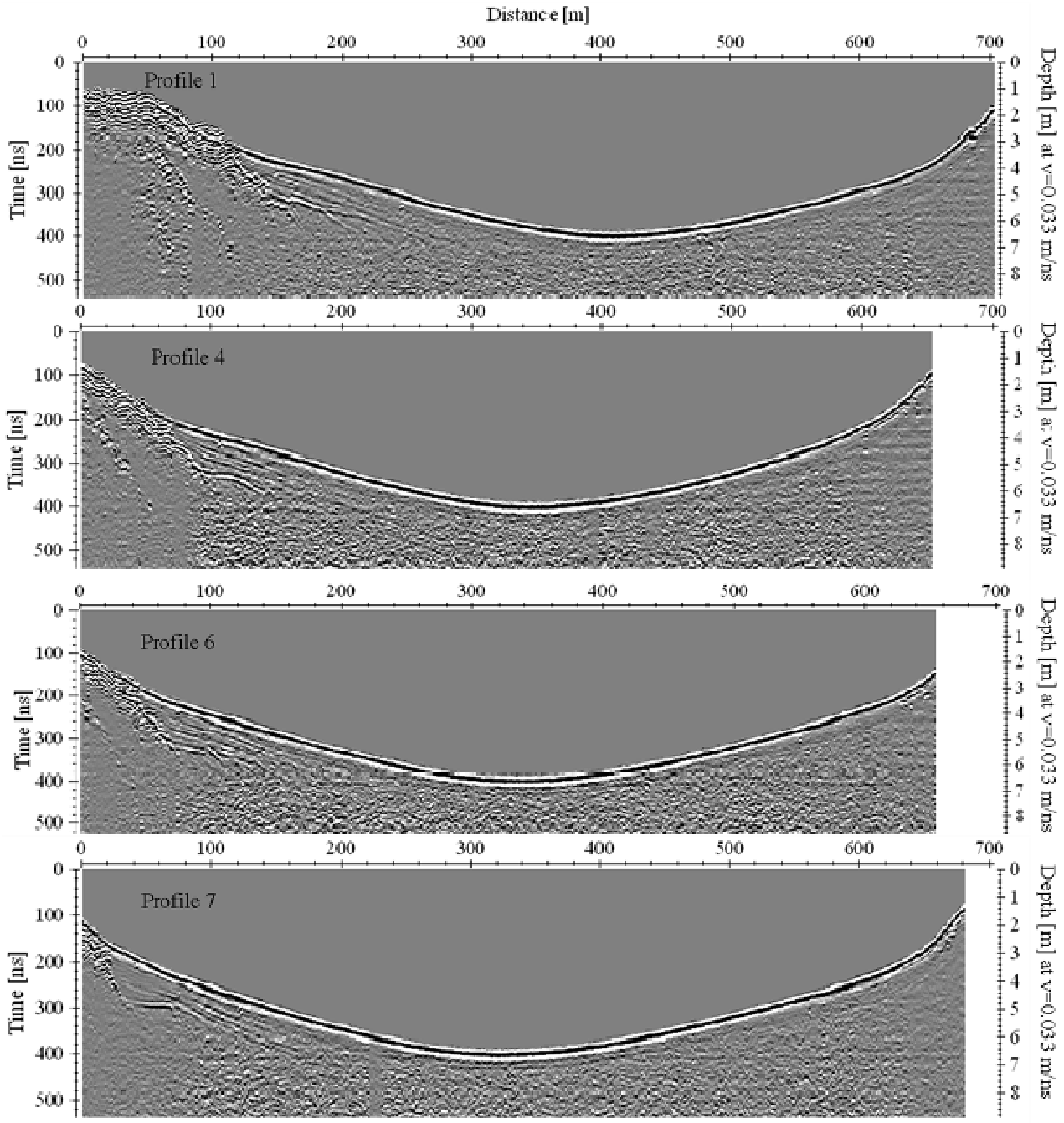
Distance [m]
Profile 1
Profile 4
Profile 6
Profile 7
Time [ns]
Depth [m] at v=0.033 m/ns

Figure 9

Figure 10

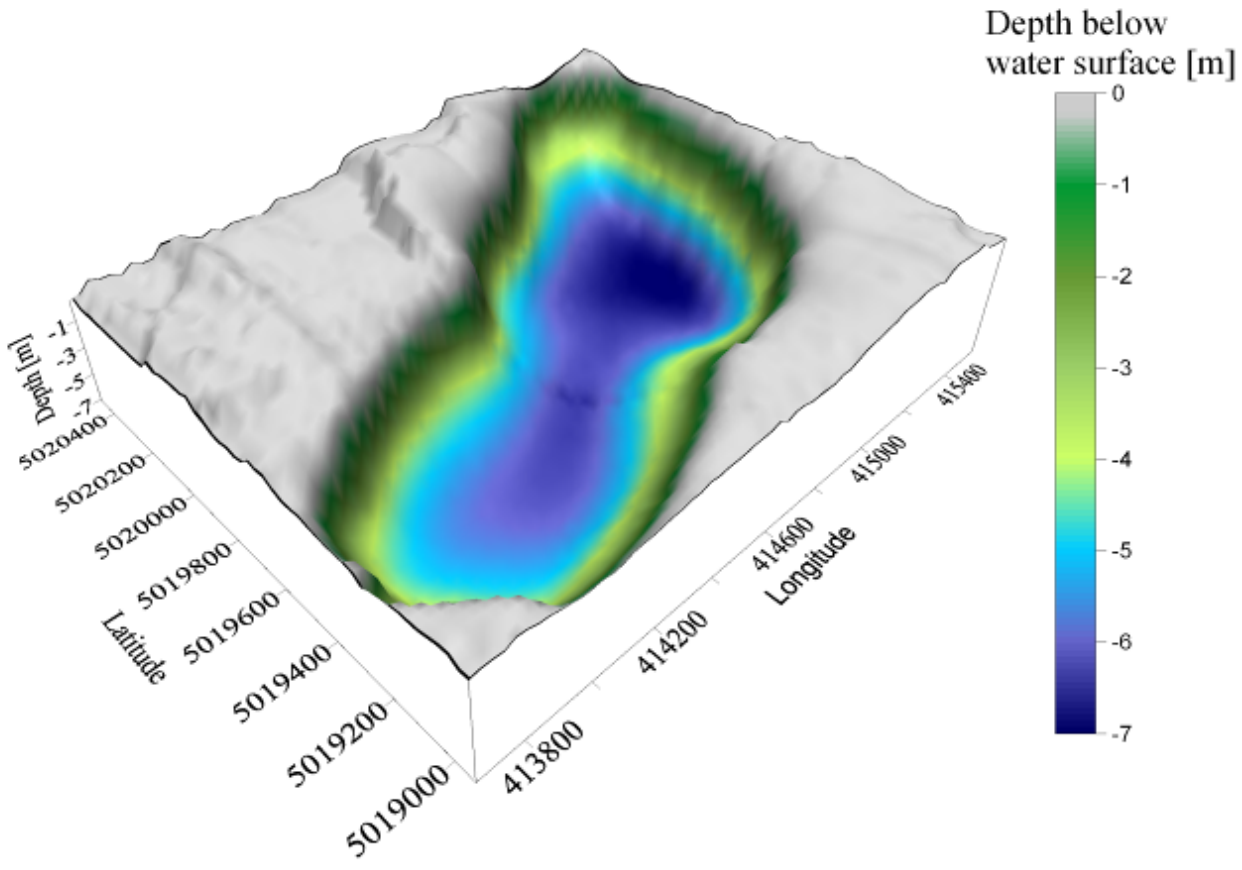

Figure 11

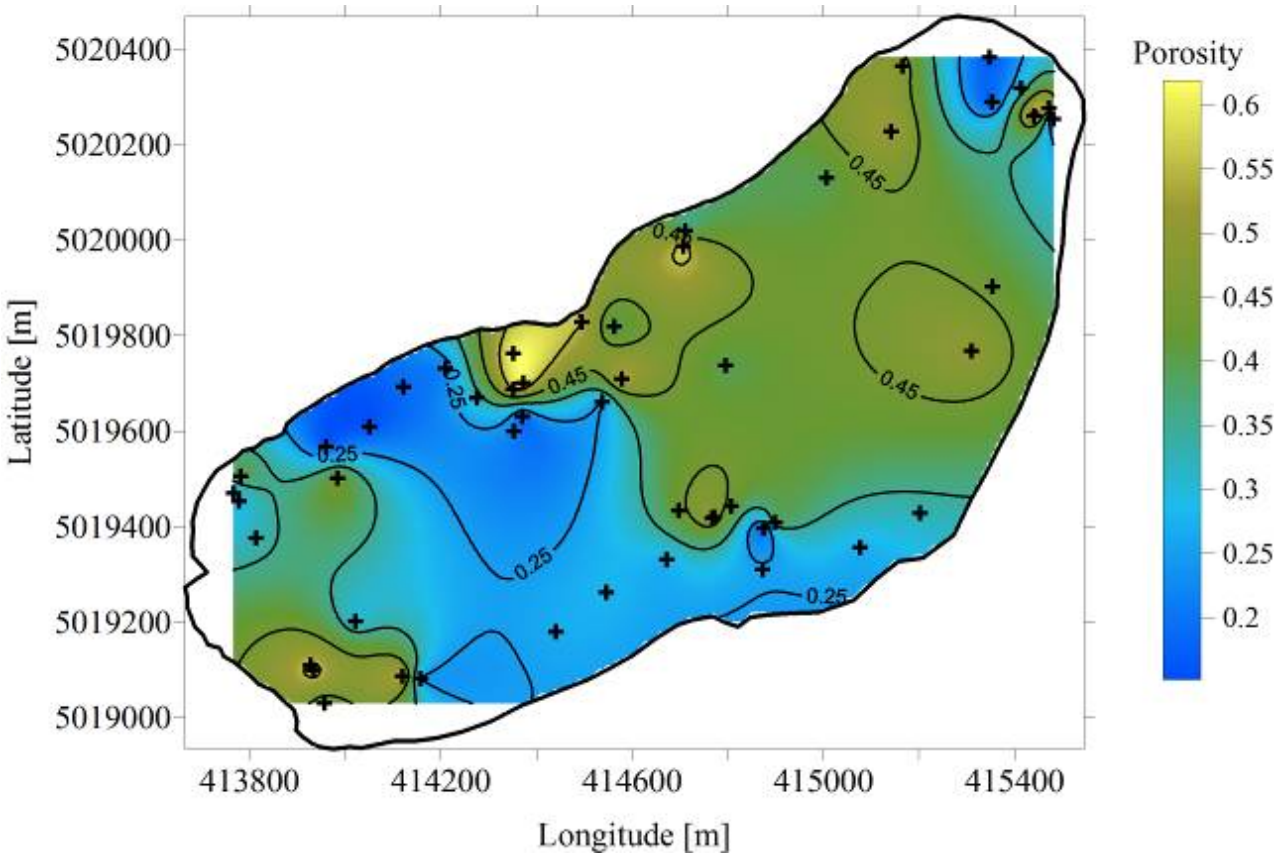
Porosity
0.6
0.55
0.5
0.45
0.4
0.35
0.3
0.25
0.2
Latitude [m]
5020400
5020200
5020000
5019800
5019600
5019400
5019200
5019000
Longitude [m]
413800
414200
414600
415000
415400
0.45
0.25

Figure 12